1   **Variable fault geometry suggests detailed fault slip-rate profiles and geometries are needed**

2   **for fault-based probabilistic seismic hazard assessment (PSHA)**

3

4   J.P. Faure Walker[1], F. Visini[2], G. Roberts[3], C. Galasso[4], K. McCaffrey[5], Z. Mildon[1,6]

5

6   [1] Institute for Risk & Disaster Reduction, University College London

7   [2] Istituto Nazionale di Geofisica e Vulcanologia

8   [3] Department of Earth and Planetary Sciences, Birkbeck College

9   [4] Department of Civil, Environmental & Geomatic University College London

10   [5] Department of Earth Sciences, Durham University, Science Labs,

11   [6] now at Centre for Research in Earth Sciences, University of Plymouth

12

13   <u>**Abstract**</u>

14   It has been suggested that a better knowledge of fault locations and slip-rates improves

15   seismic hazard assessments. However, the importance of detailed along-fault slip-rate profiles

16   and variable fault geometry has not yet been explored. We quantify the importance for modeled

17   seismicity rates of using multiple throw-rate measurements to construct along-fault throw-rate

18   profiles rather than basing throw-rate profiles on a single measurement across a fault. We use

19   data from 14 normal faults within the central Italian Apennines where we have multiple

20   measurements along the faults. For each fault, we compared strain-rates across the faults using

21   our detailed throw-rate profiles and using degraded data and simplified profiles. We show the

22   implied variation in average recurrence intervals for a variety of magnitudes that result.

23   Furthermore, we demonstrate how fault geometry (variable strike and dip) can alter calculated

24   ground shaking intensities at specific sites by changing the source-to-site distance for ground

25   motion prediction equations (GMPEs). Our findings show that improved fault-based seismic

26   hazard calculations require detailed along-fault throw-rate profiles based on well-constrained

27   local 3D fault geometry for calculating recurrence rates and shaking intensities.

28

29   **Key Words**

30   Earthquake, fault, seismic hazard, recurrence intervals, geometry, PSHA, GMPEs, Apennines

31

32   **Introduction**

33   Active fault locations and slip-rates are the principal controls on earthquake locations and

34   time-averaged recurrence rates, but fault data are currently under used within hazard assessments

35   used to calculate earthquake risk. The need for long-term fault-derived slip-rates for probabilistic

36   seismic hazard assessment (PSHA) has been noted (*e.g. Faure Walker et al., 2010; Stein et al.,*

37   *2012; Papanikolaou et al. 2015; Blumetti et al., 2017*). In particular, multi-millennia fault slip-

38   rates provide an opportunity to capture a long-term record of cumulative earthquake

39   displacements covering multiple seismic cycles and avoiding the bias introduced by temporal

40   earthquake clustering. From this average recurrence intervals can be inferred for individual

41   faults. Some researchers are incorporating long-term fault slip-rates into hazard models for

42   different regions of the world (e.g. California, USA: *Field et al., 2014*; Italy: *Valentini et al.,*

43   *2017*; Greece: *Deligiannakis et al., 2018*) and tools have been developed to help researchers with

44 such endeavors (e.g. FiSH, *Pace et al., 2016*). However, fault slip-rates remain one of the key

45 uncertainties in calculating earthquake probabilities (*Field et al., 2014*) and the lack of detailed

46 and accurate fault slip-rate data necessitates making assumptions regarding how to propagate

47 data collected at a single site along the length of the fault.

48   The problem of propagation of data along strike is clearly important, because what is known

49 from multi throw-rate and slip-rate measurements along single faults is that they are highly

50 variable; however, current fault-based approaches for calculating earthquake hazard do not

51 incorporate these detailed variations. Instead they use along-strike throw-rate or slip-rate profiles

52 with artificially assigned simplified shapes extrapolated from one to a few measurements along

53 simplified planar faults. This is in some ways inevitable because more detailed data are rarely

54 available (e.g. *Field et al., 2014*). However, detailed data are available for active normal faults

55 (e.g. *Cartwright and Mansfield, 1998; Contreras et al., 2000; Faure Walker et al., 2009; 2010;*

56 *2015; McClymont et al., 2009; Wilkinson et al., 2015; Mildon et al., 2016a; Reilly et al., 2016*)

57 and this prompts the present study where we explore the effect of along-strike throw-rate

58 variability for seismic hazard. Fortunately, locations where throw-rates vary dramatically along

59 the strike of individual faults may be easy to identify, because along-strike profiles of throw-

60 rates on active faults are altered where faults show non-planar fault geometry (*Faure Walker et*

61 *al., 2009; 2015*). Additionally, the reasons for the throw-rate variations are well-understood due

62 to development of quantitative relationships between throw-rate and fault geometry (*Faure*

63 *Walker et al., 2009; 2015; Wilkinson et al., 2015; Mildon et al., 2016a; Iezzi et al., submitted*).

64 Specifically, throw-rates are increased across bends in faults so that the strain-rates across the

65 fault remain concomitant with their position along the fault (Figure 1). The geometry-dependent

66 throw-rate model suggests active normal faults have local throw-rates governed by a

67   combination of regional-scale external forces, displacement gradients along faults, and local 3D

68   fault geometry which are inter-related (*Faure Walker et al., 2009*). The model may further

69   explain much of the scatter and variations in shape of along fault displacement profiles (e.g.

70   *Manighetti et al., 2005*) and the scatter seen in maximum slip against rupture length graphs of

71   *Wells and Coppersmith (1994)* (*Iezzi et al., submitted*). In this paper we demonstrate the effect of

72   spatial variations in throw-rate along individual faults for implied average recurrence intervals.

73   Another factor that has not been demonstrated is the compounded impact of including detailed

74   fault geometry and throw-rate measurements for calculating modeled shaking intensities. These

75   will change because along-strike bends in the map traces of faults change the distance to sites

76   where shaking intensity is of interest; where brought closer to the fault, the intensity will increase

77   and the recurrence time will decrease due to higher slip-rate, compounding the threat. We

78   emphasize that shaking intensities at given locations are a critical input for earthquake risk

79   assessment - the first step towards the development of risk reduction strategies - and

80   performance-based earthquake design. For instance, the design peak ground acceleration (PGA)

81   value for the 'ultimate limit state' or 'life-safety' performance objective is typically based on the

82   annual rate of exceedance of 1/475 (corresponding to a mean return period of 475 years) (e.g.,

83   the current Italian Building Code, or IBC08, see *Iervolino et al., 2011*) and this will be affected

84   by distance to the fault traces that rupture. This is because GMPEs, also known as ground-

85   motion models and attenuation relations, are typically used to model the intensity of shaking at

86   individual sites and across an area, within the framework of PSHA. GMPEs are empirical models

87   estimating the probability distribution of ground-motion intensity measures (IMs) - such as PGA

88   and SA (spectral acceleration) - occurring at a given site as a function of magnitude, source-to-

89   site distance between the seismic source (the fault) and the site of interest, soil properties at the

90   site, focal mechanism, and other parameters (e.g. *Bindi et al., 2011*). The source-to-site distance

91   can be measured using a variety of metrics, such as R_{jb} ("Joyner-Boore" distance), R_{rup} (slant

92   distance), R_{cent} (centroid distance), R_{hyp} (hypocentral distance), and R_{epi} (epicentral distance), see

93   for instance *Bommer and Akkar (2012)*. To be computed in practice and be used in hazard

94   assessments, these metrics require knowledge of the fault location and dip. For example, R_{jb}, is

95   the closest horizontal distance from the site to the vertical projection of the rupture surface,

96   which is dependent on the surface trace of the fault and the dip of the fault. Even if most modern

97   GMPEs use definitions of the source-to-site distance that reflect the dimensions of the fault

98   rupture for larger earthquakes rather than using point-source measures relative to the epicenter or

99   hypocenter, the role of variable fault strike and a change of dip along strike are generally not

100   considered in GMPEs used for hazard calculations or in the other steps of PSHA. In this paper

101   we show that detailed knowledge of strike-variable fault geometries changes calculated shaking

102   intensities, a critical input for PSHA.

103   The background to our emphasis on using detailed fault slip-rate and fault geometry data is

104   that most seismic hazard models currently used by government civil protection agencies to

105   inform building codes and emergency planning, and by the (re)insurance industry, are driven by

106   historical earthquake data and by the definition of seismic source zones, or areal sources, i.e., all

107   the points within the considered area can be the epicenter of earthquakes with the same

108   probability (e.g. *Stucchi et al., 2011*). This is in spite of it being known that historical and

109   seismological records are of insufficient length relative to average fault recurrence intervals to be

110   representative of longer time periods and capture the geography of seismic hazard (e.g.

111   *Camelbeeck et al., 2007; Stein et al., 2012; Liu and Stein, 2016; Blumetti et al., 2017*). In

112   particular, in continental settings, faults exist that are capable of producing large magnitude

113   earthquakes that have not ruptured in historical times (e.g., *Liu et al., 2011; Mildon et al., 2017;*

114   *Hintersberger et al. 2018*). For instance, in the central Apennines, Italy, the historical records are

115   restricted to hundreds of years, but individual faults have recurrence intervals of hundreds to

116   thousands of years (e.g. *Pace et al., 2006; Galli et al., 2008*). In August and October 2016, three

117   earthquakes Mw 5.9 - 6.5 ruptured the Mt. Vettore fault (e.g. *Livio et al., 2016; Cheloni et al.,*

118   *2017; Pucci et al., 2017; Civico et al., 2018; Villani et al., 2018*), a known active mapped fault

119   that had not ruptured within the historical record but had clear evidence of meter-scale Holocene

120   slip events (*Galadini and Galli, 2003; Mildon et al., 2017*; *Wedmore et al., 2017*). PSHA based

121   on the historical record prior to these events would not explicitly include the hazard from this

122   fault, or others that have not ruptured during historical times. Other examples worldwide such as

123   the 2011 Great East Japan Earthquake and the 2010 Haiti Earthquake have had their probability

124   underestimated because the fault displacement-rates were not properly considered (*Stein et al.,*

125   *2012*). At a scale larger than individual faults, the pitfalls of using only shorter-term historical

126   and seismicity data or deformation rates derived from geodesy to infer hazard have been

127   highlighted in continental settings such as the central Italian Apennines *(Faure Walker et al.,*

128   *2010)* and North China (*Liu et al., 2011*). For example, in the central Italian Apennines,

129   calculated long-term (15±3kyr) fault-derived strain-rates in polygons with areas in the order of

130   1,000km^2 do not match short-term strain-rates inferred from historical moment tensors (700yrs)

131   and geodesy (126yrs) (*Faure Walker et al., 2010*). The short-term (700yr) strain-rates are lower

132   than long-term (15±3kyr) strain-rates in some areas but higher in others (*Faure Walker et al.,*

133   *2010*). This leads to dramatic underestimations and overestimations of hazard for those areas

134   respectively if calculated solely from historical records (*Faure Walker et al., 2010*). Without the

135   longer-term view, hazard assessments will continue to be biased by the most recent events and

136 hence risk from faults that have not ruptured in recent or historical times will not be

137 communicated (e.g. *Liu and Stein, 2016*).

138   In this paper, we first calculate strain-rates and average recurrence intervals for a fault where

139 data on detailed along-strike variations in throw-rate are available, and then demonstrate how

140 degrading detailed along-strike throw-rate profiles to simplified idealized along-strike throw-rate

141 profiles affects the calculated strain-rate across a single fault. We then expand this investigation

142 to 14 individual faults for which we have moderately detailed data. For our example fault we

143 show how the simplifications to the throw-rate profile affect average recurrence intervals

144 calculated using FiSH software (*Pace et al., 2016*). For another example fault, we investigate the

145 effect of simplifying fault map geometry and throw-rate profiles on expected shaking intensities.

146 We find that detailed fault throw-rate profiles and fault geometries can have significant impact

147 on calculated recurrence rates and ground shaking intensities at specific sites. Therefore, we

148 argue that such variations should be considered within uncertainties of fault-based probabilistic

149 seismic hazard assessments.

150

151 **Geological Background**

152   The studied faults are located in the central Apennines, Italy, a region of extending

153 continental crust where offset 15±3ka landforms and sediments can be used to constrain throw-

154 rates across normal faults (Figure 2) (e.g. *Piccardi et al., 1999; Roberts and Michetti, 2004*).

155 Evidence for the age of the offset landforms and sediments comes from tephrachronology, ^{36}Cl

156 cosmogenic exposure dating of fault scarps and upper slopes, the timing of a change from

157 periglacial processes dominating slopes along active faults to slopes controlled by surface fault

158 slip, and shifts in δ^{18}O from Tyrrhenian and other Mediterranean sea cores (*Giraudi and*

159   *Frezzotti, 1986; Giraudi & Frezzotti, 1997; Allen et al., 1999; Cowie et al., 2017*). Average

160   15±3ka fault throw-rates can be derived from topographic profiles across the offset slopes (e.g.

161   *Roberts and Michetti, 2004*). This time period covers multiple seismic cycles (e.g. *Palumbo et*

162   *al., 2004; Galli et al., 2008; Cowie et al., 2017*). 15ka throw-rates are representative of even

163   longer time periods demonstrated by calculated strain-rates averaged over 15±3ka correlating

164   with total fault throws across the faults developed since 2-3Ma, mantle SKS splitting delay

165   times, and elevation above sea-level via a power law with exponent ~3 (*Faure Walker et al.,*

166   *2012; Cowie et al., 2013*). This supports the idea that average recurrence intervals derived from

167   15±3ka rates are stable for even longer time periods. A map of the active faults in the region is

168   shown in Figure 3 with the 14 faults investigated in this study highlighted.

169

Methods

171   We show the relevance for earthquake hazard calculations of using detailed or degraded data

172   for a single fault, and then for 14 studied normal faults in the central Italian Apennines. We

173   calculate strain-rates across each of these faults using detailed measurements of fault strike, dip

174   and throw-rate. We compare the results to strain-rates calculated across the same 14 faults, but

175   assuming planar fault geometry and taking a single measurement of the throw-rate and using this

176   value to create assumed, simplified along-strike throw-rate profiles assuming either a 'boxcar' or

177   'triangular' profile (examples shown in Figure 4b). Using an example fault for each, we compare

178   the detailed and degraded data cases for modeled average recurrence intervals and annual rates of

179   exceeding specified ground shaking intensities.

180   Previously published data, supplemented by new fieldwork data (Table 1), of fault throws,

181   and slip vector azimuths and plunges were used for the fault geometry, slip vectors and throw-

182 rates needed as inputs to strain-rate calculations (Figure 2) (*Morewood and Roberts, 2000;*

183 *Roberts and Michetti, 2004; Papanikolau et al., 2005; Papanikolau and Roberts, 2007; Faure*

184 *Walker et al., 2009; 2010; 2012; Wilkinson et al., 2015; Cowie et al., 2017; Mildon, 2017;*

185 *Wedmore, 2017*). The selected faults were mapped using field mapping, digital elevation models,

186 satellite imagery, SRTM (Shuttle Radar Topography Mission) data, geological maps and

187 paleoseismic trench data (*Roberts and Michetti, 2004; Roberts, 2008; Faure Walker et al., 2009;*

188 *2010; 2012; Cowie et al., 2017*). Topographic profiles across exposed fault scarps constraining

189 the throw-rate at multiple sites along the faults have been constructed using slope angles

190 measured directly in the field (Figure 2, see *Faure Walker et al., 2010* for a review of the

191 method). At selected sites topography profiles have been extracted from DEMs constructed from

192 terrestrial LiDAR scanning (see *Wilkinson et al., 2015* and *Cowie et al., 2017* for a review of the

193 method). Slip vectors were determined by averaging measurements of multiple slickensides at

194 each site on the exposed limestone fault planes (Figure 2).

195 The strain-rate across each of the 14 individual faults was calculated building on methods

196 developed by *Faure Walker et al. (2009, 2010)*. The method combines measurements of fault

197 strike, dip, throw, length and slip vector azimuth and plunge to calculate moment tensors using

198 adaptations of the *Kostrov (1974)* equations. To capture the local variations in fault geometry

199 and throw-rates, we discretized each non-planar fault on a regular grid with individual grid boxes

200 having dimensions of 1km x 2km and calculated strain-rates on planar segments confined within

201 each grid box. For the strain-rate across each whole fault (which vary in length between 5.5km

202 and 46km) we combine grid squares to model the non-planar fault.

203 For each of the 14 studied faults we have at least four measurements of throw (one fault has

204 30 measurements while the remaining 13 faults have eleven or less) to contribute to the detailed

205   or 'all data' case. We remove data points for the degraded data cases. For example, for the

206   Parasano-Pescina fault, we have seven data sites along the fault with values for the 15ka throw,

207   geometry (strike and dip) and slip-vector (Figure 4a). To investigate the effect of using degraded

208   data, we compare calculations of strain-rate across this fault using (i) all data sites in the 'all

209   data' throw profile with degraded data: (ii) leaving out the maximum throw point in the 'no max'

210   profile but including the other measurements; (iii-) extrapolating a single throw along the whole

211   fault in a 'boxcar' profile; and (iv) extrapolating throw along the fault by decreasing the

212   maximum throw linearly to the fault tips in a 'triangular' profile (Figure 4b,c). We present three

213   'boxcar' scenarios: (iii-1) 'boxcar-max' which extrapolates the maximum throw along the whole

214   fault; (iii-2) 'boxcar-mean' for which we integrate the throw profile to find the average

215   displacement and extrapolate this along the whole fault; and (iii-3) 'boxcar-min' for which we

216   extrapolate the minimum measured throw along the whole fault. For cases (i) and (ii) we use the

217   detailed fault geometry, but for cases (iii) and (iv) we assume a planar fault geometry. We

218   calculate strain-rates across a further 13 faults for the 'all data', 'boxcar-max', 'boxcar-mean',

219   'boxcar-min' and 'triangular' throw profiles.

220   To demonstrate the effect of using degraded data for calculating earthquake rates, we

221   calculate recurrence intervals for two of the faults: the Parasano-Pescina Fault and the

222   Pescasseroli fault. The earthquake magnitude-frequency distributions have been modeled with a

223   truncated Gutenberg-Richter relationship using the FiSH software (*Pace et al., 2016*). In this

224   distribution, the *b*-value describes how the number of events with magnitude ≥*M*, *N*, changes

225   with magnitude up to a threshold magnitude, above which *N* decreases more rapidly (*Kagan,*

226   *2002; Jackson & Kagan; 2006*). For this study, *b* is assumed to be 1 (following *Bird and Kagan,*

227   *2004; Valentini et al., 2017*). The maximum earthquake magnitudes (*Mmax*) of the truncated

228   Gutenberg-Richter relationship for each fault have been calculated using empirical relationships

229   based on fault length (*Wells and Coppersmith, 1994*).

230   To calculate activity rates at magnitudes given by the truncated Gutenberg-Richter

231   relationship, we balanced the expected seismic moment rate of the truncated Gutenberg-Richter

232   relationship with the seismic moment rate obtained by geometry and slip rates ($\dot{M}_g$):

233     $$M_g = \dot{\mu} LWV \qquad\qquad (1)$$

234   where μ is the shear modulus, V is the slip rate, and L and W are along-strike rupture length

235   and downdip width, respectively. In this study, to include slip rate variability along strike, as

236   well as detailed slip rate profiles, we assumed:

237     $$M_g = \mu \sum L_i W_i V_i \qquad\qquad (2)$$

238   where i indicates data of along-strike segments of a fault.

239   The effect of using degraded data on expected ground shaking at individual sites was

240   investigated through a site-specific PSHA. We calculate annual rates of exceeding specified

241   ground shaking intensities at a specified site. Earthquake rates for different earthquake

242   magnitudes are calculated as described above using the 'all data', 'boxcar-max' and 'triangular'

243   throw profiles. Shaking intensities for given magnitudes are calculated using GMPEs.

244   We use the widely-applied GMPEs for Italy (*Bindi et al., 2011*) to calculate the ground

245   shaking from earthquakes on the Pescasseroli fault at a given site several kilometers from the

246   fault. These GMPEs are derived for the geometrical mean of the horizontal components and the

247   vertical, considering the latest release of the strong motion database for Italy. The regressions are

248   performed over the magnitude range 4–6.9 and considering distances up to 200 km. The

249   equations are derived for PGA, peak ground velocity (PGV) and 5%-damped spectral

250   acceleration (SA) at periods between 0.04 and 2 s.

251   To test the effect of using simplified fault geometries on expected ground shaking intensities,

252   we compare the GMPE results basing the source-to-site distance on detailed fault geometry and

253   simplified planar fault geometries. Consistent with the used GMPEs, we use the R_{jb} source-to-

254   site distance. For the 'all data' throw profile, we use R_{jb} based both on detailed fault geometry

255   and simplified planar geometries. The simplified geometries use a planar fault strike projected

256   between the two fault tips and two different fault dips: one using the fault dip measured at the

257   site of maximum throw and the other using the fault dip measured at the fault tip. For the

258   'triangular' and 'boxcar-max' throw-profiles, the two planar fault geometries are modeled.

259   We account for uncertainty in the factors affecting ground motions by using a Monte Carlo

260   simulation-based approach (e.g. *Assatourians and Atkinson, 2013*). To this aim, a 10,000yrs

261   synthetically generated set of potential earthquakes across the Pescasseroli Fault, with their

262   temporal distribution, is developed by drawing random samples from the assumed PSHA model

263   components (and related probability distributions), i.e., magnitude-recurrence parameters and

264   maximum magnitude, as defined above. 500 realizations of random numbers drawn from the

265   standard normal distribution is multiplied by the given sigma value (variability of the GMPE

266   model) and added to the median log-ground motions (from the GMPEs) to model the aleatory

267   variability in ground motions. Site-specific hazard curves are displayed showing annual rates of

268   exceedance against PGA and SA(1s). For the 'all data' throw profile with the strike-variable

269   fault geometry, we show hazard curves of the PGA for each realization as well as the median,

270   16th and 84th curves (representing ±1σ). For all the simplified cases only the median curve is

271   shown. In general, SA(1s) can be used as good predictor of the structural response and induced-

272   damage of low-to-mid rise buildings, one of the most common construction types in Italy (e.g.,

273   *Rosetto et al., 2016*).

274

275   **<u>Results</u>**

276   The strain-rates within individual 1km x 2km grid boxes across the Parasano-Pescina fault are

277   shown in Figure 4. Figure 4(i) shows the strain-rates calculated using all the data. Figures 4(ii-iv)

278   show how the calculated strain-rates across the whole fault change for the 'no max', 'boxcar-

279   max', 'boxcar-mean', 'boxcar-min' and 'triangular' throw profiles to 93%, 158%, 104%, 61%

280   and 78% of the 'all data' profile respectively (the bars and errors of the 'all data' case are shown

281   on each graph). The strain-rates calculated across the fault using the 'boxcar-max' (iii-1),

282   'boxcar-min' (iii-3) and 'triangular' (iv) throw profiles are outside the error margins of the

283   calculated strain-rate across the fault using all the available data (i).

284   In Figure 5, the calculated strain-rates for the 'all data', 'boxcar-max', 'boxcar-mean',

285   'boxcar-min' and 'triangular' throw profiles are compared for each of the 14 studied faults. The

286   strain-rates for each fault are normalized to the 'all data' case to allow comparison between the

287   calculated strain-rate and the scenarios modeled with simplified throw-rate profiles. For the

288   simplified 'boxcar-max', 'boxcar-mean', 'boxcar-min' and 'triangular' throw profiles, only one,

289   nine, two and three of the faults have strain-rates within the 'all data' case errors respectively

290   (errors for strain-rates across entire faults using 'all data' vary between 6% and 20%). Strain-

291   rates across faults for the simplified cases vary from 51% to 303% relative to the 'all data' cases

292   and half of them have calculated strain-rates <0.5 or >1.5 times the 'all data' cases. The results in

293   Figures 4 and 5 demonstrate that one measurement of throw extrapolated along strike in either a

294   'boxcar' or 'triangular' profile is insufficient to characterize strain-rates across a fault.

295   The effect of using degraded data on calculated recurrence intervals is shown for the

296   Parasano-Pescina fault in Figure 6. The different throw profiles modify the implied $\geq M_w 5.1$

297   average earthquake recurrence intervals from 420yrs ('all data') to 465yrs, 262yrs and 524yrs for

298   the 'no max', 'boxcar-max', and 'triangular' throw profile cases respectively.

299   Figure 7 shows site-specific spectral shaking for an example fault can be altered beyond the

300   1σ uncertainty if a simplified fault geometry is assumed that does not include strike-variable

301   geometry. We show the shaking derived from using our measured, detailed fault geometry and

302   two examples of simplified planar fault geometry to demonstrate this point. We use an example

303   site, which has Rjb distance to the Pescasseroli fault of 4.6km when utilizing the detailed fault

304   trace and measurements of dip. However, this distance in increased to 6.4km and 11.3km if the

305   fault is simplified to having planar geometry between the tips with the dip projected from the

306   maximum throw site and tip respectively (see Figure 7a). Figure 7b shows how degrading the

307   fault geometry - so that the fault becomes planar - changes calculated ground shaking from that

308   fault at the specified example site by altering the source-to-site distance (solid line compared to

309   dashed and dotted lines). Figure 7c shows the combined effect of degrading both the fault

310   geometry and throw profiles (dotted and dashed lines). For this fault, the 475yr return period

311   PGA for a given site varies from 0.23g (±1σ: 0.21-0.24g) given the actual fault geometry to

312   0.20g or 0.13g when relying on simplified tip-to-tip planar fault geometries with the dip

313   projected from the maximum throw data site or from the fault tip respectively. If the simplified

314   throw profiles are added to the simplified planar fault geometries for this example fault, this

315   reduces the 475yr PGA to as low as 0.12g (52% of the 'all data' case using detailed geometry)

316   compared to the 0.23g (±1σ: 0.21-0.24g) for the actual fault geometry and detailed throw dataset,

317   a difference that is bigger than the uncertainty on the latter. This is because a fault's non-

14

318   planarity alters the fault-to-site distance and simplified throw profiles change calculated rates of

319   occurrence. A similar result can be observed in terms of SA(1s) (Figure 7). The observed

320   discrepancies in the observed shaking intensities between simplified and detailed fault geometry

321   further increase at higher mean return periods (lower annual rates of exceedance) (Figure 7c).

322

323   **<u>Discussion</u>**

324   Constraining slip-rate has been cited as one of the key uncertainties in earthquake probability

325   calculations (*Field et al., 2014*). For example, in California UCERF3 slip-rates are directly

326   constrained for less than half the fault segments (*Field et al., 2014*). Detailed data showing how

327   throw-rates and fault geometry vary along a fault are rarely available. Therefore, how these

328   parameters change along the length of a fault generally needs to be inferred from just one or a

329   few measurements. For fault-based PSHA the importance of using such extrapolations needs to

330   be known. In this paper we show that key outputs from fault-based PSHA vary dramatically if

331   the inferred along-strike throw-rate (and hence slip-rate) profile is in error.

332   For our degraded data sets used for calculating recurrence intervals and ground shaking, we

333   included the data we considered most likely to be present in a less detailed dataset, in other

334   words, the long-term throw data most likely to be collected when only one or a few

335   measurements are taken to represent the throw along the entire fault. We considered the case

336   where only one data site exists along the fault and extrapolated this using 'boxcar-max' and

337   'triangular' throw profiles. In these two scenarios, we assumed that the most likely location

338   where data may be collected would be the site of maximum offset due to it being the most likely

339   site to have identifiable and preserved offset features. In addition, for an example fault we

340   studied the effect of a scenario where detailed data has been collected, but not from the site of

341   maximum throw: the 'no max' case (ii). In the studied fault, the maximum offset occurs across a

342   bend in the fault, as expected from the geometry-dependent throw-rate model in *Faure Walker et*

343   *al. (2009, 2015)*, so this degraded data scenario represents a case where the bend is not

344   identified, leading to exclusion of a site of higher throw. We show this example to highlight the

345   importance of ensuring data is not excluded along locations with variable geometry. The strain-

346   rate calculated using the integrated average throw does lie within the 'all data' case error for nine

347   of the 14 faults, however, for five of the faults an average throw is insufficient. We emphasize

348   that in general fewer measurements than what we have are available for calculating an average

349   throw and hence using average throw-rates or slip-rates will likely cause worse results than

350   shown. We have not determined a general rule as to whether using average throw-rates would

351   more likely overestimate or underestimate the strain-rate across a fault because it is dependent on

352   which throw-rate measurements are incorporated in the calculation of the average throw-rate. We

353   show the 'boxcar-min' and 'boxcar-max' scenarios to demonstrate the range of possible values

354   that could be obtained from using an "average" throw-rate when this is calculated from fewer

355   data points. Therefore, we argue that using an "average" throw or slip projected along the fault is

356   also insufficient for modeling hazard.

357   If the problems with extrapolating data are not recognized, this can lead to large errors in

358   recurrence interval calculations. To put this into perspective we discuss how this compares to the

359   effect of temporal variability in the recurrence intervals due to earthquake clustering. Values of

360   the coefficient of variation (CV, standard deviation of the recurrence interval divided by the

361   mean recurrence interval) generally used in PSHA are <0.5 as this is consistent with values

362   computed (e.g. 0.38 (*Gonzalez et al., 2006*); 0.14-0.34 (*Pace et al., 2006*); 0.48 (*Lienkaemper*

363   *and Williams, 2007*); 0.2-0.39 (*Visini and Pace, 2014*)). Half our strain-rates calculated using the

364   simplified throw-rate scenarios lead to values <0.5 or >1.5 times the 'all data' case; this

365   demonstrates that using detailed throws changes probability calculations beyond the uncertainty

366   due to intrinsic natural variability.

367   We also demonstrate that if the compounded effect of using simplified planar fault geometry

368   and simplified throw profiles on calculated ground shaking exceedance probabilities is not

369   considered, this will lead to errors in values that inform building code regulations. For the

370   example Pescasseroli fault, the 475yr return period PGA is altered beyond 1σ error and thus our

371   results are significant, for instance, to building code 'ultimate limit state' and 'life-safety'. The

372   observed differences further increase at higher mean return periods, for instance for the 2475yr

373   PGA or SA(1s), corresponding to collapse prevention in several international building codes and

374   in the IBC08. For other faults, whether ground shaking calculated from simplified throw-rates

375   and planar geometries is higher or lower than the 'all data' case will depend on both the impact

376   on the recurrence intervals and changes in modeled source-to-site distances. To what extent and

377   to how far from a fault the calculated ground shaking could be impacted by performing

378   calculations based on simplified planar fault geometry and a simplified throw or slip profile is

379   likely to be a function of how variable the actual fault geometry is. Note that local calculations in

380   shaking intensities near faults could be further altered where there are dramatic local variations

381   in fault strike. For instance, along a strongly non-planar fault such as the Fiamignano fault

382   (Figure 3), planar fault models could underestimate local shaking intensities by mislocating a site

383   from the hangingwall onto the footwall. Therefore, the non-planarity of faults, detailed changes

384   in throw-rates along faults and local dramatic changes in fault strikes could have significant

385   impact for local planning and disaster management through building regulation impacts. At a

386   regional scale, changes in implied exceedance probabilities of implied shaking (PGA or SA) will

387 have impact on the calculated damage state and hence calculated losses in catastrophe models

388 used within the insurance industry. To achieve high-resolution risk mapping, detailed fault

389 parameters need to be included.

390 We note that a full hazard analysis could use a combination of GMPEs, through a logic-tree

391 approach (e.g. *Bommer et al., 2005*). These should include epistemic uncertainties such as site-

392 specific properties and dip propagation with depth. However, in this paper we use just one set of

393 GMPEs to demonstrate the relevance of geometry. The *Bindi et al. (2011)* GMPEs were chosen

394 because they perform well in the region. Specifically, they performed better than older GMPEs

395 for calculating predicted shaking intensities at stations following the 24th August 2016 Amatrice

396 earthquake (*Meletti et al., 2016*; *EEFIT, 2017*).

397 Most hazard assessments (for earthquakes and other natural hazards) are at a lower spatial

398 resolution than would be desirable for planners (e.g. *Pile et al., 2018*); this is particularly

399 pertinent in areas with critical infrastructure and highly populated areas. Fault-derived hazard

400 maps allow seismic hazard to be calculated at a high spatial resolution (e.g. *Deligiannakis et al.,*

401 *2018*). However, a balance has to be achieved between increasing resolution and any

402 accompanying increases in uncertainty, so understanding how a lack of detailed fault knowledge

403 affects fault-based hazard calculations and associated uncertainties is needed. We have shown

404 herein that calculating exceedance probabilities of shaking intensities at a high spatial resolution

405 requires detailed throw-rate and geometry measurements as simplifying these can create results

406 beyond 1σ uncertainty. Therefore, we advocate the use of fault data to increase resolution, but

407 with caution of including appropriate uncertainties where detailed data is lacking. In contrast to

408 fault-based hazard assessments, those based solely on historical shaking or instrumental

409 seismicity data have a restricted resolution because they divide the catalogue of earthquakes

410   amongst seismic source zones (e.g., *Meletti et al., 2008*). These are polygons drawn on maps

411   enclosing large areas with similar historical seismicity. Fault traces are not used, but instead the

412   polygons represent areas that enclose one or more suspected seismic sources. Earthquake

413   probabilities are calculated in each polygon using the rate of historical seismicity (e.g. *Meletti et*

414   *al., 2008*). It is the size of these polygons that limits the spatial resolution of the hazard maps,

415   which in turn is limited by the available historical or seismicity data.

416   We have not determined herein what spatial resolution of throw-rate data is required for

417   resolving the along-strike throw-rate profiles of faults with sufficient detail to capture the

418   variations in throw-rates such that more measurements do not change inferred recurrence

419   intervals. In terms of resolving individual paleoearthquake magnitudes along a fault from trench

420   sites, *Hintersberger and Decker (2015)* found that 4-6 observation sites were required. We have

421   used at least 4 sites along each fault in our analysis to represent the 'all data' cases for the 14

422   faults studied, equivalent to measurements with average inter-site spacing of 200m to 6km. The

423   geometry-dependent throw-rate model (*Faure Walker et al., 2009; 2015*) suggests that faults

424   with a higher along-strike variation in geometry would likely have a corresponding greater

425   variation in throw-rate along the strike. This might suggest that using simplified throw-rate

426   profiles is sufficient if faults are relatively planar (e.g. *D'Amato et al., 2017*), but not if the fault

427   has more variable fault geometry. This has not been tested, but intuitively it is clear that more

428   sites are needed for faults with greater non-planarity. To determine the required spatial

429   resolution, we need a greater number of examples of faults with multiple data sites.

430   Currently such detailed geometry and throw-rate data with multiple data points on each fault

431   is not available and in some areas it may be difficult to obtain it by ground-based field methods.

432   However, we note that techniques to capture such data - such as TLS (terrestrial laser scanning),

433 ALS (airborne LiDAR scanning) and structure from motion photogrammetry - are making the

434 data acquisition increasingly possible (e.g. see *Telling et al. (2017)* for a review of improvements

435 in modeling fault geometries with TLS). With increasing capabilities to measure such detail we

436 argue that as such data become available they should be used. In addition, throw-rates can be

437 constrained from paleoseismic trench studies. However, such studies need to use multiple sites

438 along a fault and consider fault geometry when extrapolating point data along a fault or input

439 into calculations like those in *Faure Walker et al. (2009)* so that along strike variations in throw-

440 rate can be calculated relative to constrained sites.

441 In addition to including detailed geometry for calculating earthquake rates and ground

442 shaking intensities, we suggest that it should also be used for other aspects of hazard

443 calculations. For example, the effect of Coulomb stress transfer is sometimes included in

444 earthquake probability calculations (e.g. *Pace et al., 2014*). We note that there are increasing

445 capabilities to input fault geometry detail in Coulomb stress transfer calculations, with existing

446 studies demonstrating the need for strike-variable geometry (*Mildon et al. 2016b; 2017*).

447 Overall, we argue that fault slip-rates are needed to inform seismic hazard calculations rather

448 than relying on historical records alone, however we have demonstrated herein the importance of

449 using detailed along-fault throw-rate profiles and detailed fault geometry for these. Without such

450 data, hazard calculations used to inform government, industry, and residents may misinform

451 about the geography of seismic hazard and hence not trigger appropriate action to mitigate

452 against future events. Our results highlight that local 3D fault geometry and local throw-rates

453 must be considered when extrapolating data from individual sites along a fault for use in fault-

454 based PSHA. We have demonstrated the importance of detailed data for calculating strain-rates

455 and hence earthquake moment release across faults (*Faure Walker et al., 2009; 2010; Wilkinson*

456   *et al., 2015*), earthquake recurrence intervals averaged over multiple earthquake cycles, and

457   expected shaking calculated using GMPEs. For individual towns, multiple faults will affect the

458   probabilities of different shaking intensities so the changes for the individual faults shown here

459   will be compounded. Therefore, we are advocating a change in how fault slip-rates and geometry

460   are considered in PSHA calculations.

461

462   **<u>Conclusions</u>**

463   We find that using detailed fault throw profiles and fault geometries that vary along strike

464   can have significant impact on calculated hazard calculations by altering recurrence rates and

465   ground shaking intensities at specific sites respectively. We show that probability calculations

466   change beyond the uncertainty due to intrinsic natural variability and site-specific shaking

467   intensities change beyond the uncertainty bounds of GMPEs. Therefore, we argue that either

468   detailed data should be used when calculating hazard or that such variations should be

469   considered within uncertainties of fault-based PSHA.

470   We studied 14 active normal faults within the central Apennines for which we have four or

471   more sites constraining the post 15ka throw-rate. Calculating strain-rates across these faults from

472   simplified 'boxcar-max', 'boxcar-mean', 'boxcar-min' and 'triangular' throw profiles resulted in

473   only one, nine, two and three of the faults having strain-rates lie within 1 sigma error of the 'all

474   data' case respectively. For the simplified cases, calculated strain-rates vary from 51% to 303%

475   relative to the 'all data' cases with half of them having calculated strain-rates <0.5 or >1.5 times

476   the 'all data' cases. These results demonstrate how far from the actual rates simplifications can

477   cause the strain-rates to be.

478   For an example fault, the Parasano-Pescina fault, using simplified throw-rate profiles modifies

479   the implied $\geq M_w 5.1$ average earthquake recurrence intervals from 420yrs ('all data') to 465yrs,

480   262yrs and 524yrs for the 'no max', 'boxcar-max', and 'triangular' throw profile cases

481   respectively.

482   For another example fault, the Pescasseroli fault, the 475yr return period PGA for a given site

483   a few kilometers (R_{jb} 4.6km) from the fault varies from 0.41g (±1σ: 0.37-0.44g) given the actual

484   fault geometry and throw-profile to 0.34g or 0.24g when relying on simplified tip-to-tip planar

485   fault geometries with the dip projected from the maximum throw site or from the fault tip

486   respectively. Using simplified throw profiles and planar fault geometries for this example fault

487   alters the 475yr PGA to as low as 0.19g (46% of the 'all data' case using detailed geometry).

488

489   **Data and Resources**

490   The data used in this paper came from published sources listed in the references and new data

491   in Table 1. Figure 3 was made using the Generic Mapping Tools version 5.2.1

492   (www.soest.hawaii.edu/gmt; Wessel and Smith, 1998).

493

498

499   **References**

500

501   Allen J., Brandte U., Brauer A., Hubbertens H.-W., Huntley B., Keller J., Kraml M., Mackensen

502   A., Mingram J., Negendank J., et al., 1999, Rapid environmental changes in southern Europe

503   during the last glacial period, Nature, 400, 740–743

504

505   D'Amato D., Pace B., Di Nicola L., Stuart F.M., Visini F., Azzaro R., Branca S., Barford D.N.

506   (2017) Holocene slip rate variability along the Pernicana fault system (Mt. Etna, Italy): Evidence

507   from offset lava flows, GSA Bulletin 129 (3-4) 304-317

508

509   Assatorians K. and Atkinson G.M. (2013) EqHaz: An Open-Source probabilistic seismic-hazard

510   code based on the Monte Carlo simulation approach, *Seismological Research Letters,* 84 (3),

511   516-524, DOI 10.1785/0220120102

512

513   Bindi D., Pacor F., Luzi L., Puglia R., Massa M., Ameri G., Paolucci R., (2011), Ground Motion

514   Prediction Equations derived from the Italian strong motion database, Bulletin of Earthquake

515   Engineering, 9 (6) 1899-1920

516

517   Bird P. and Kagan Y.Y., (2004), Plate-Tectonic Analysis of Shallow Seismicity: Apparent

518   Boundary Width, Beta, Corner Magnitude, coupled Lithosphere Thickness, and Coupling in

519   Seven Tectonic Settings, Bulletin of the Seismological Society of America, 94 (6), 2380-2399

520

521 Blumetti A.M., Grutzner C., Guerrieri L. and Livio F., (2017), Quaternary earthquakes: Geology

522 and palaeoseismology for seismic hazard assessment, Quaternary International, 451, 1-10

523

524 Bommer J.J. and Akkar S., (2012) Consistent Source-to-Site Distance Metrics in Ground-Motion

525 Prediction Equations and Seismic Source Models for PSHA, *EARTHQUAKE SPECTRA*, 28, 1-

526 15, ISSN: 8755-2930

527

528 Bommer J.J., Scherbaum F., Bungum H., Cotton F., Sabetta F., Abrahamson N.A. (2005), On the

529 use of Logic Trees for Ground Motion Prediction Equations in seismic hazard analysis, *Bulletin*

530 *of the Seismological Society of America,* 95 (2) 377-389, DOI:10.1785/0120040073

531

532 Camelbeeck, T., Vanneste, K., Alexandre, P., Verbeeck, K., Petermans, T., Rosset, P., Everaerts,

533 Warnant, R., and van Camp, M., (2007) Relevance of active faulting and seismicity studies to

534 assessments of long-term earthquake activity and maximum 20 magnitude in intraplate northwest

535 Europe, between the Lower Rhine Embayment and the North Sea. Geol. Soc. Am. Spec. Pap.

536 425, 193-224

537

538 Cartwright J.A. and Mansfield C.S., (1998), Lateral displacement variation and lateral tip

539 geometry of normal faults in the Canyonlands National Park, Utah, *Journal of Structural*

540 *Geology,* 20 (1) 3-19

541

542 Cheloni D., De Novellis V., Albano M., Antonioli A., Anzidei M., Atzori S., Avallone A.,

543 Bignami C., Bonano M., Calcaterra S., et al., (2017) Geodetic model of the 2016 Central Italy

544 earthquake sequence inferred from InSAR and GPS data, *Geophysical Research Letters,* 44,

545 6778–6787, doi:10.1002/2017GL073580.

546

547 Civico R, Pucci S, Villani F, Pizzimenti L, De Martini PM, Nappi R, and the Open EMERGEO

548 Working Group (2018) Surface ruptures following the 30 October 2016 Mw6.5 Norcia

549 earthquake, central Apennines, *Journal of Maps,* 151-160 DOI:

550 10.1080/17445647.2018.1441756

551

552 Contreras J., Anders M.H., and Scholz C.H. (2000) Growth of a normal fault system:

553 observations from the Lake Malawi basin of the east African rift, *Journal of Structural Geology*,

554 22, 159-168

555

556 Cowie P., Scholz C., Roberts G., Faure Walker J.P., Sheer P. (2013) Viscous roots of active

557 seismogenic faults revealed by geologic slip rate variations, *Nature Geoscience*, 6, 1036-1040

558

559 Cowie PA, Phillips RJ, Roberts GP, McCaffrey K, Zijerveld LJJ, Gregory LC, Faure Walker JP,

560 Wedmore LNJ, Dunai TJ, Binnie SA, et al., (2017) Orogen-scale uplift in the central Italian

561 Apennines drives episodic behaviour of earthquake faults, *Scientific Reports,* 7,

562 doi:10.1038/srep44858

563

564 Deligiannakis G., Papanikolaou I.D., Roberts G., 2018, Fault specific GIS based seismic hazard

565 maps for the Attica region, Greece, *Geomorphology*, 306 264-282, ISSN 0169-555X

566

567 Faure Walker, J.P., Roberts, G.P., Cowie, P.A., Papanikolaou, I., Michetti, A.M., Sammonds, P.,

568 Phillips, R., (2009). Horizontal strain-rates and throw-rates across breached relay-zones, central

569 Italy: implications for the preservation of throw deficits at points of normal fault linkage, *Journal*

570 *of Structural Geology* 31 1145-1160 doi:10.1016/j.jsg.2009.06.011

571

572 Faure Walker, J.P. (2010) Mechanics of Continental Extension in the Italian Apennines, *PhD*

573 *Thesis, University College London*

574

575 Faure Walker, J.P., Roberts, G.P., Sammonds, P., Cowie, P.A.C., (2010). Comparison of

576 earthquake strains over 100 and 10,000 year timescales: insights into variability in the seismic

577 cycle in the central Apennines, Italy. Journal of Geophysical Research 115 (B10418)

578 doi:10.1029/2009JB006462.

579

580 Faure Walker, J.P., Roberts, G.P., Cowie, P.A., Papanikolaou, I., Michetti, A.M., Sammonds, P.,

581 Wilkinson M., McCaffrey K. & Phillips R. (2012) Relationship between topography, rates of

582 extension and mantle dynamics in the actively-extending Italian Apennines, *Earth and Planetary*

583 *Science Letters* 325-326, 76-84

584

585   Faure Walker, J.P., Roberts, G.P., Cowie, P.A., McCaffrey K., Wedmore L., Watson Z., Gregory

586   L., (2015) Long-term strain rates as a tool for understanding the mechanics of continental

587   extension and the importance of local 3D fault geometry for local throw-rates across faults. *6th*

588   *Int. INQUA Meeting on Paleoseismology, Active Tectonics and Archaeoseismology, 19-24 April*

589   *2015*, Pescina, Fucino Basin, Italy, *Miscellanea INGV ISSN 2039-6651 2015_Numero* 27 150-

590   154

591

592   Field G. P. Biasi G.P., Bird P., Dawson T.E., Felzer K.R., Jackson D.D., Johnson K.M., Jordan

593   T.H., Madden C. Michael A.J., et al., (2014). Uniform California Earthquake Rupture Forecast,

594   Version 3 (UCERF3) - The time-independent model, *Bulletin of the Seismological Society of*

595   *America* 104 (3) 1122–1180, doi:10.1785/0120130164

596

597   Galadini, F. and Galli, P., (2003) Paleoseismology of silent faults in the Central Apennines

598   (Italy): the Mt. Vettore and Laga Mts. faults, *Annals of Geophysics*, 46(5), 815–836.

599

600   Galli, P., F. Galadini, and D. Pantosti (2008), Twenty years of paleoseismology in Italy, *Earth*

601   *Science Reviews*, 88, 89–117.

602

603   Giraudi C. and Frezzotti M., Inversione pleistocenica del drenaggio in alta Val Roveto (Abruzzo

604   sud occidentale) (1986), *Mem. Soc. Geol. It.,* 35, 847-853

605

606 Giraudi G. and Frezzotti M., (1997) Late Pleistocene Glacial Events in the Central Apennines,

607 Italy, *Quaternary Research*, 48, 280-290

608

609 Gonzalez, A., J. B. Gomez, and A. F. Pacheco (2006). Updating seismic hazard at Parkfield,

610 *Journal of Seismology* 10 (2) 131–135

611

612 Hintersberger E. and Decker K. (2015), Estimating magnitudes of paleo-earthquakes from

613 multiple observations, *6th Int. INQUA Meeting on Paleoseismology, Active Tectonics and*

614 *Archaeoseismology, 19-24 April 2015*, Pescina, Fucino Basin, , Italy, *Miscellanea INGV ISSN*

615 *2039-6651 2015_Numero* 27 207-208

616

617 Hintersberger E., Decker K., Lomax J., Luthgens C. (2018) Implications from

618 palaeoseismological investigations at the Markgrafneusiedl Fault (Vienna Basin, Austria) for

619 seismic hazard assessment, *Natural Hazards and Earth Systems,* 18, 531-553, doi:

620 10.5194/nhess-18-531-2018

621

622 Iervolino I., Galasso C., Paolucci R., Pacor F. (2011) Engineering ground motion record

623 selection in the Italian Accelerometric Archive. *Bulletin of Earthquake Engineering*, 9(6):1761-

624 1778.

625

626   Iezzi F., Mildon Z., Faure Walker J.P., Roberts G., Goodall H., Wilkinson M., Robertson J.,

627   Coseismic throw variation across along-strike bends on active normal faults: implications for

628   displacement/length scaling of seismic rupture, *submitted manuscript*

629

630   Jackson D.D. and Kagan Y.Y., (2006) The 2004 Parkfield earthquake, the 1985 prediction, and

631   characteristic earthquakes: Lessons for the future, *Bulletin of the Seismological Society of*

632   *America* 96 (4B), S397-S409

633

634   Kagan Y.Y. (2002) Seismic moment distribution revisited: I. Statistical results, *Geophysical*

635   *Journal International* 148 520-541

636

637   Kostrov V.V., (1974) Seismic Moment and Energy of Earthquakes, and Seismic Flow of Rock,

638   Izv., Earth Physics,1, 23-40 (translation UDC 550.341, 13-21)

639

640   Lienkaemper, J. J., and P. L. Williams (2007). A record of large earthquakes on the southern

641   Hayward fault for the past 1800 years, *Bulletin of the Seismological Society of America* 97 (6)

642   1803–1819, doi: 10.1785/0120060258.

643

644   Liu M., Stein S., and Wang H., (2011), '2000 years of migrating earthquakes in North China:

645   How earthquakes in midcontinents differ from those at plate boundaries' *Lithosphere*, vol 3, no.

646   2, pp. 128-132. DOI: 10.1130/L129.1

647

648   Liu M. and Stein S., (2016) Mid-continental earthquakes: Spatiotemporal occurrences, causes,

649   and hazards *Earth-Science Reviews*, 162, 364-386

650

651   Livio F., A.M. Michetti, E. Vittori, L. Gregory, L. Wedmore, L. Piccardi, E. Tondi, G. Roberts,

652   A.M. Blumetti, L. Bonadeo, F. et al., Surface faulting during the August 24, 2016, Central Italy

653   earthquake (Mw 6.0): preliminary results, (2016) *Annals of Geophysics*, 59 (5), DOI:

654   10.4401/ag-7197

655

656   Manighetti, I., M. Campillo, C. Sammis, P.M. Mai and G. King, (2005). Evidence of self-similar,

657   triangular slip distributions on earthquakes: Implications for earthquakes and fault mechanics.

658   *Journal of Geophysical Research*. 110, B05302.

659

660   McClymont A.F., Villamor P. and Green A.G. (2009) Fault displacement accumulation and slip

661   rate variability within the Taupo Rift (New Zealand) based on trench and 3-D ground-penetrating

662   radar data, *Tectonics* 28 (4), DOI: 10.1029/2008TC002334

663

664   Meletti C., Galadini F., Valensise G., Stucchi M., Basili R., Barba S., Boschi E., (2008) A

665   seismic source zone model for the seismic hazard assessment of the Italian territory,

666   *Tectonophysics*, 450, 1-4, 85-108

667

668   Meletti C., Visini F., D'Amico V., Rovida A. (2016), Seismic Hazard in Central Italy and the

669   2016 Amatrice earthquake, Annals of Geophysics, 59 DOI: 10.4401/AG-7248

670

671   Mildon Z.K., Roberts G., Faure Walker J.P., Iezzi F. (2017), Coulomb stress transfer and fault

672   interaction over millennia on non-planar active normal faults: the Mw 6.5-5.0 seismic sequence

673   of 2016-2017, central Italy, *Geophysical Journal International* 210 (2) 1206-1218

674

675   Mildon Z.K., Roberts G., Faure Walker J.P., Wedmore L., McCaffrey K. (2016a) Active normal

676   faulting during the 1997 seismic sequence in Colfiorito, Umbria: Did slip propagate to the

677   surface? *Journal of Structural Geology* 91 102-113

678

679   Mildon Z.K., Toda S., Faure Walker J.P., Roberts G. (2016b), Evaluating models of Coulomb

680   stress transfer - is variable fault geometry important? *Geophysical Research Letters* 43

681

682   Mildon Z. K., (2017) The link between earthquakes and structural geology; the role of elapsed

683   time, 3D geometry and stress transfer in the central Apennines, Italy. *Doctoral thesis, UCL*

684   *(University College London)*

685

686   Morewood N.C. and Roberts G.P., (2000) The geometry, kinematics and rates of deformation

687   within an en echelon normal fault boundary, central Italy, Journal of Structural Geology, 22,

688   1027-1047

689

690 Pace, B., L. Peruzza, G. Lavecchia, and P. Boncio (2006). Layered seismogenic source model

691 and probabilistic seismic-hazard analyses in central Italy, *Bull. Seism. Soc. Am.* 96 (1) 107 –132

692

693 Pace, B., Bocchini G.M., Boncio P., (2014) Do static stress changes of a moderate-magnitude

694 earthquake significantly modify the regional seismic hazard? Hints from the L'Aquila 2009

695 normal-faulting earthquake (Mw 6.3, central Italy), *Terra Nova*, 26 430-439, DOI:

696 10.1111/ter.12117

697

698 Pace B., Visini F., Peruzza L., (2016) *FiSH*: MATLAB Tools to Turn Fault Data into Seismic

699 Hazard Models, *Seismological Research Letters*, DOI: 10.1785/0220150189

700

701 Palumbo, L., Benedetti L., Bourles D., Cinque A., and Finkel R., (2004), Slip history of the

702 Magnola fault (Apennines, central Italy) from 36Cl surface exposure dating: evidence for strong

703 earthquakes over the Holocene, *Earth and Planetary Science Letters*, 225, 163–176.

704

705 Papanikolaou I.D., Roberts G.P., and Michetti A.M., (2005) Fault scarps and deformation rates

706 in Lazio-Abruzzo, Central Italy: Comparison between geological fault slip-rate and GPS data,

707 Tectonophysics, 408, 147-176, 2005

708

709 Papanikolaou I.D. and Roberts G.P., (2007) Geometry, kinematics and deformation rates along

710   the active normal fault system in the southern Apennines: Implications for fault growth, Journal

711   of Structural Geology, 29, 166-188, 2007

712

713   Papanikolaou I.D., Van Balen R., Silva P.G., Reicherter K. (2015) Geomorphology of active

714   faulting and seismic hazard assessment: New tools and future challenges, Geomorphology 237 1-

715   13

716

717   Piccardi L., Gaudemer Y., Tapponier P., and Boccaletti M., (1999) Active oblique extension in

718   the central Apennines (Italy): evidence from the Fucino region, Geophysical Journal

719   International, 139, 499-530

720

721   Pile J., Gouramanis C., Switzer A.D., Rush B., Reynolds I., Soria J.L.A. (2018) Can the risk of

722   coastal hazards be better communicated? *International Journal of Disaster Risk Reduction*, 27,

723   439-450

724

725   Pucci, S., De Martini P.M., Civico R., Villani F., Nappi R., Ricci T., Azzaro R., Brunori C.A.,

726   Caciagli M., Cinti F.R. et al. (2017), Coseismic ruptures of the 24 August 2016, M_w 6.0 Amatrice

727   earthquake (central Italy), Geophys. Res. Lett., 44, 2138–2147, doi:10.1002/2016GL071859.

728

729   Reilly C., Nicol A. and Walsh J., (2016) Importance of pre-existing fault size for the evolution of

730   an inverted fault system, *Geological Society, London, Special Publications,* 439, 447-463 DOI:

731   10.1144/SP439.2

732

733   Roberts, G.P., Michetti, A.M., (2004) Spatial and temporal variations in growth rates along

734   active normal fault systems: an example from the Lazio-Abruzzo Apennines, central Italy. *J.*

735   *Struct. Geol.* 26, 339–376.

736

737   Rosetto, T., Gehl, P., Minas, S., Galasso, G., Duffour P., Douglas, J., and Cook, O., (2016)

738   FRACAS: A capacity spectrum approach for seismic fragility assessment including record-to-

739   record variability, *Engineering Structures*, 125 337-348, doi: 10.1016/j.engstruct.2016.06.043

740

741   Stein, S., R. Geller, and M. Liu (2012), Why earthquake hazard maps often fail and what to do

742   about it, *Tectonophysics*, 562–563, 1–25.

743

744   Stucchi M., Meletti C., Montaldo V., Crowley H., Calvi G.M., Boschi E., (2011) Seismic Hazard

745   Assessment (2003-2009) for the Italian Building Code, *Bulletin of the Seimsmological Society of*

746   *America*, DOI: 10.1785/0120100130

747

748   Telling J., Lyda A., Hartzell P., Glennie C., (2017) Review of Earth science research using

749   terrestrial lasar scanning, *Earth Science Reviews*, 169 35-68

750

751   Valentini, A., Visini, F., and Pace, B.: (2017) Integrating faults and past earthquakes into a

752 probabilistic seismic hazard model for peninsular Italy, *Natural Hazards and Earth Science*

753 *Systems*, 17 (11), doi: 10.5194/nhess-17-2017-2017

754

755 Villani F, Civico R, Pucci S, Pizzimenti L, Nappi R, De Martini PM, and the Open ERERGEO

756 Working Group (2018), A database of the coseismic effects following the 30 October 2016

757 Norcia earthquake in Central Italy, *Scientific Data*, 5, doi:10.1038/sdata.2018.49

758

759 Visini, F., and Pace, B. (2014) Insights on a key parameter of earthquake forecasting, the

760 coefficient of variation of the recurrence time, using a simple earthquake simulator,

761 *Seismological Research Letters*, 85 (3) 703–713, doi:10.1785/0220130165.

762

763 Wedmore W., Faure Walker J.P., Roberts G., Sammonds P., McCaffrey K., Cowie C. (2017) A

764 667 year record of coseismic and interseismic Coulomb stress changes in central Italy reveals the

765 role of fault interaction in controlling irregular earthquake recurrence intervals, *Journal of*

766 *Geophysical Research*, 122 (7) 5691-5711

767

768 Wedmore, LNJ; (2017) Fault interaction processes and continental extension in the central

769 Apennines, Italy. *Doctoral thesis, UCL (University College London)*

770

771 Wells D.L. and Coppersmith K.J. (1994) New empirical relationships among magnitude, rupture

772 length, rupture width, rupture area and surface displacement, *Bulletin Seismological Society of*

773 *America* 84 974-1002

774

775   Wessel, P., W. H. F. Smith, R. Scharroo, J. F. Luis, and F. Wobbe, (2013) Generic Mapping

776   Tools: Improved version released, *EOS Trans. AGU*, 94, 409-410

777

778   Wilkinson, M., Roberts, G.P. , McCaffrey, K.J.W., Cowie, P.A., Faure Walker, J.P.,

779   Papanikolaou, I.D., Phillips, R.J., Michetti, A.M., Vittori, E. , Gregory, L., et al., (2015) Slip

780   distributions on active normal faults measured from LiDAR and field mapping of geomorphic

781   offsets: an example from L'Aquila, Italy, and implications for modelling seismic moment release,

782   *Geomorphology* 237 130-141

783

Full Mailing List of Each Author (alphabetically)

785

786   Joanna Faure Walker − Institute for Risk & Disaster Reduction, University College London,

787   Gower Street, London, WC1E 6BT

788   Carmine Galasso − Department of Civil, Environmental & Geomatic Engineering, University

789   College London, London, Gower Street,WC1E 6BT, UK

790   Ken McCaffrey - Department of Earth Sciences, Durham University, Science Labs, Durham

791   DH1 3LE UK

792   Zoe Mildon −Centre for Research in Earth Sciences, University of Plymouth, Drake Circus,

793   Plymouth, Devon, PL4 8AA

794   Gerald Roberts − Department of Earth and Planetary Sciences, Birkbeck College, Malet Street,

795   London, WC1E 7HX, UK

796   Francesco Visini - Istituto Nazionale di Geofisica e Vulcanologia, Via della Faggiola, 32, 56126

797   – Pisa, Italy

798

799   **Tables**

800   Table 1: Fieldwork data used within calculations that have not been previously published.

Fault	UTM X	UTM Y	Slip vector azimuth (°)	Slip vector plunge (°)	15ka throw (m)
Barisciano	369075	4698111	194	51	7.0
	383475	4689190			6.5
	392297	4679321	226	44	6.5
Fucino	393474	4644538	229	52	
	393493	4644535	233	58	
	393541	4644520	209	56	
	393583	4644506	210	58	
	393594	4644503	219	59	
	393636	4644489	220	50	
	393736	4644447	218	40	
Liri	364529	4648418	168	65	

	364554	4648395	173	61	
	364628	4648319	178	67	9
	364633	4648332	189	71	
	364671	4648294	197	64	
	364683	4648271	189	66	
	364722	4648213	177	58	
Ocre	367652	4682645	197	66	
	367884	4682479			6.4
	368647	4681804	211	58	
	368775	4681715	213	46	
	368838	4681676	217	56	
	368939	4681589			2.8
	369008	4681532	260	62	
	369048	4681494	255	55	6.3 ±3.0 *(eye estimate)*
	369068	4681487			4.0
	369251	4681334	217	54	
Roccapreturo	392123	4672914	185	62	
	393537	4671944	237	47	

	393541	4671945			6.5
	393554	4671926	231	50	
	393665	4671836	225	57	
	393699	4671804	215	55	
	393781	4671481	215	59	
	393785	4671635	211	44	
	393791	4671445	213	56	
	393799	4671404	212	53	
	393971	4671229			8.47
	393995	4671211	258	45	
	394004	4671182	258	55	
	395036	4670693	253	52	
Scanno	406678	4642989	209	41	
	406796	4643001			4.5
	406929	4642938	217	47	10.6
	407154	4642786			12.6
	407413	4642561	224	58	
	407452	4642544	217	52	12.3

	407462	4642521	228	54	
	407571	4642414	212	52	
	410765	4637903			4.0

801

802 **<u>Figure captions</u>**

3D Cartoon showing an idealised schematic
of a fault scarp containing a fault bend

The fault has a steeper dip and greater
throw across the fault bend

Main fault strike

Bend in fault strike

- - - Line of constant displacement
⌐ Strike and Dip
⟍ Slip
⟍ Extra slip across bend

Greater throw,
steeper dip

Main fault strike

Plan view of fault section
with a bend in strike

Slip vector

Slip vector remains consistent across fault bend in this example

Throw across displayed fault section
assuming strain-rate remains concomitant with position along fault

Throw
(m)

The Geometry-dependent throw-rate model predicts a higher throw-rate
where there is a bend in the fault strike

Distance (m)

Strain-rate across displayed fault section

Strain
rate
(ppm/yr)

In this example the strain-rate is constant across the centre of the fault
and then decreases gradually towards the tip

Distance (m)

Figure 1: Geometry-dependent throw-rate model. The figure shows how, for a given strain-rate

profile, the throw-rate across the fault changes with a change in strike along the fault. In order

to keep the strain-rate concomitant with its position along a fault, the throw-rate varies where

there are changes in fault strike and dip. How the strain-rate changes along the fault is shown

41

808   *here for one idealized example. The figure has been adapted from Faure Walker et al. (2015).*
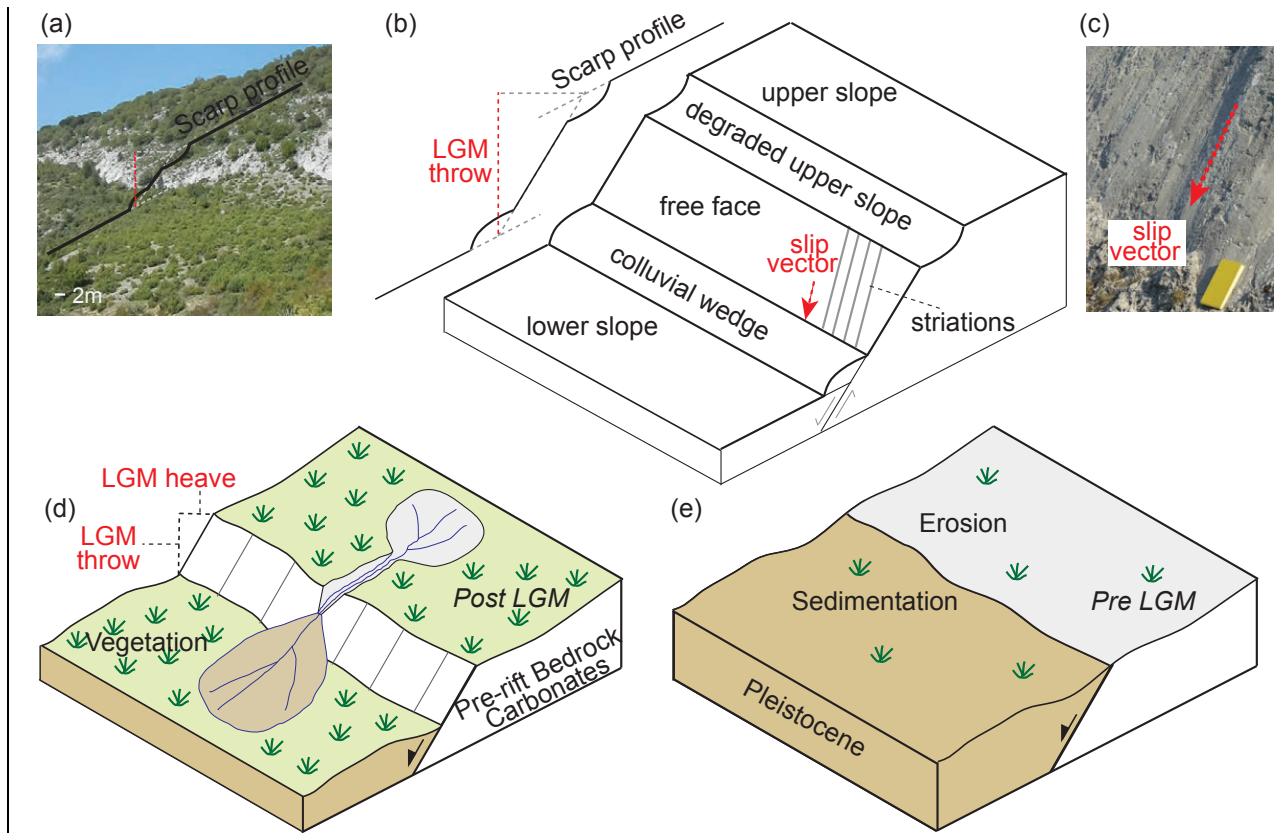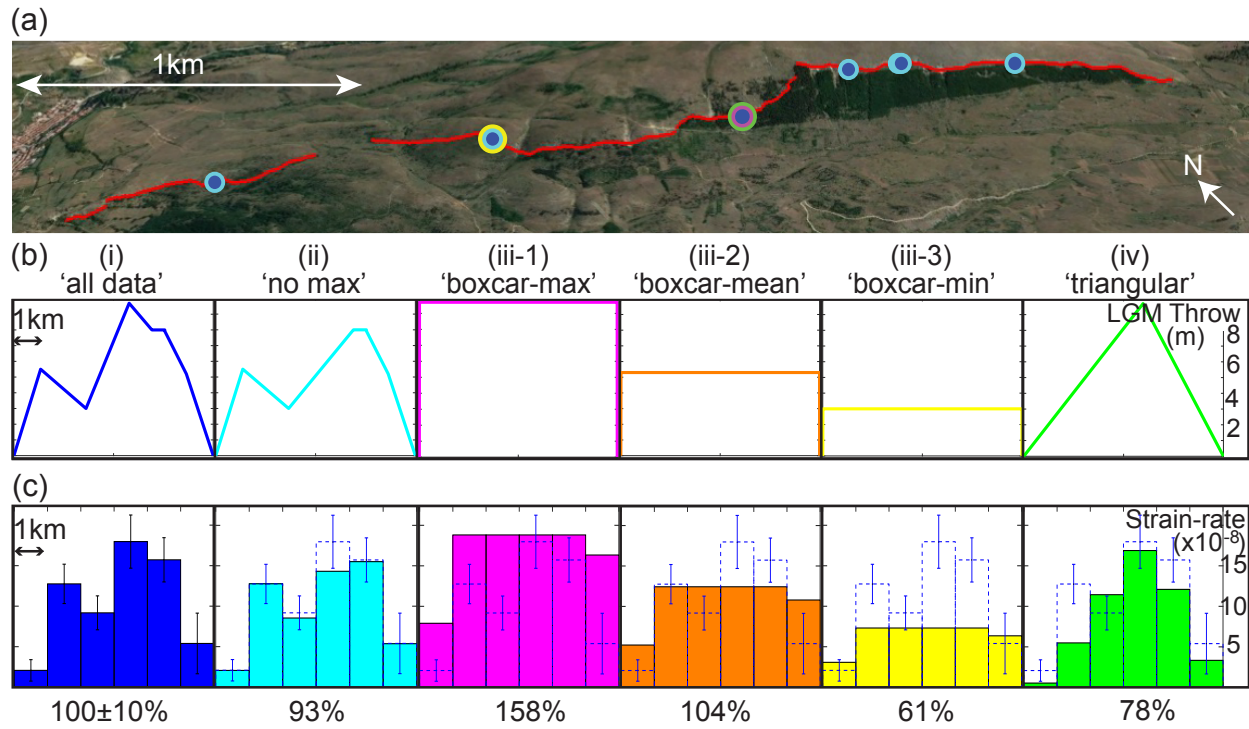

810   *Figure 2: Fault scarps exposed at the surface in the central Italian Apennines formed since the*

811   *end of the LGM (Last Glacial Maximum). (a) Photograph of a post glacial scarp with example of*

812   *a scarp profile line. (b) Cartoon topographic scarp profile constructed across cartoon fault*

813   *scarp showing how the throw since the LGM is constructed. (c) Striations on limestone fault*

814   *plane revealing slip vector (d) Cartoon showing formation of surface scarp following the LGM,*

815   *the scarp is exposed because fault slip-rates are faster than erosion and sedimentation rates; the*

816   *LGM provides a time marker since the scarps were formed because during the glacial maximum,*

817   *as shown in (e), scarps were generally not exposed as erosion and sedimentation rates*

818   *outstripped fault slip rates. (b) adapted from Faure Walker et al. (2009), (d) and (e) adapted*

819   *from Roberts and Michetti (2004) and Faure Walker (2010).*
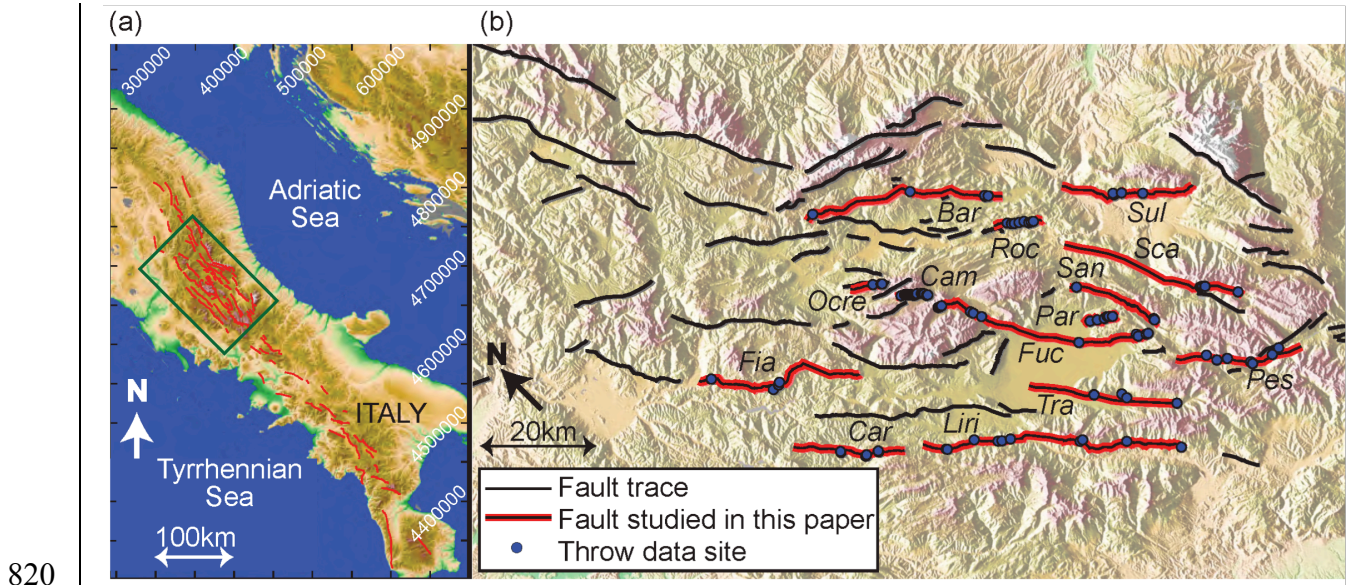
Figure 3: Map of the active faults in the central Apennines study region showing studied faults. The box in location map (a) shows the area covered by the more detailed map (b) of the 14 faults investigated in this study. Along the 14 faults, which are highlighted in red, sites with 15ka throw-rate measurements are shown with filled in circles. Bar=Barisciano, Cam=Campo Felice, Car=Carsoli, Fia=Fiamignano, Fuc=Fucino, Par=Parasano, Pes=Pescasseroli, Roc=Roccapreturo, San=San Sebastiano, Sca=Scanno, Sul=Sulmona, Tra=Trasacco. Liri and Ocre also marked. Figures produced using GMT (Wessel et al., 2013).

(a)

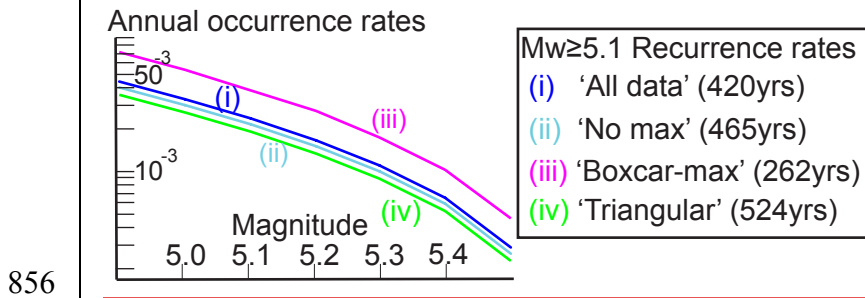1km

N

(b)
| (i) 'all data' | (ii) 'no max' | (iii-1) 'boxcar-max' | (iii-2) 'boxcar-mean' | (iii-3) 'boxcar-min' | (iv) 'triangular' |

1km

LGM Throw (m)
8
6
4
2

(c)

1km

Strain-rate (x10^{-8})
15
10
5

| 100±10% | 93% | 158% | 104% | 61% | 78% |

828

Figure 4: Plots show how 15kyr strain-rates in a regular 1x2km grid change along the

Parasano-Pescina fault and how using degraded data for the throw profiles affects the

calculated strain-rates across the fault. (a) Trace of Parasano-Pescina Fault from

GoogleEarth^{TM}. Circles show sites of post-glacial throw measurements, the colours correspond

to which models (i-iv) the throw measurements were used in. (b) Throw profiles along the fault

for each of the models and (c) strain-rates within 1km x 2km grid boxes along the fault. (i) 'all

data' uses all the data from the seven data collection sites along the fault. (ii) 'no max' uses all

the data except from the throw-rate data collected from the site of maximum 15ka throw. (iii-1)

'boxcar-max' only uses the data from the maximum throw-rate site, (iii-2) 'boxcar-mean' uses

the average 15ka throw, slip vector azimuth and plunge, and (iii-3) 'boxcar-min' uses only data

collected from the minimum throw-rate site (above zero). In each 'boxcar' scenario, the value of

throw is projected along the entire length of the fault until near the fault tips where the throw

rapidly decreases to zero. (iv) 'triangular', like 'boxcar-max' only uses the data from the

829
830
831
832
833
834
835
836
837
838
839
840
841

842 *maximum throw-rate site, but in this scenario the throw-rate decreases linearly from the*

843 *maximum to zero at each tip forming a triangular throw-rate profile along the fault. Error bars*

844 *and dotted bar plots shown in each plot are for the 'all data' case (i). Percentage values in the*

845 *boxes give the total strain-rate across the fault relative to the 'all data' case (i). This shows that*

846 *degrading data by excluding a single data point (ii) or extrapolating a single throw value along*

847 *a fault (iii, iv) changes calculated strain-rates across the fault.*
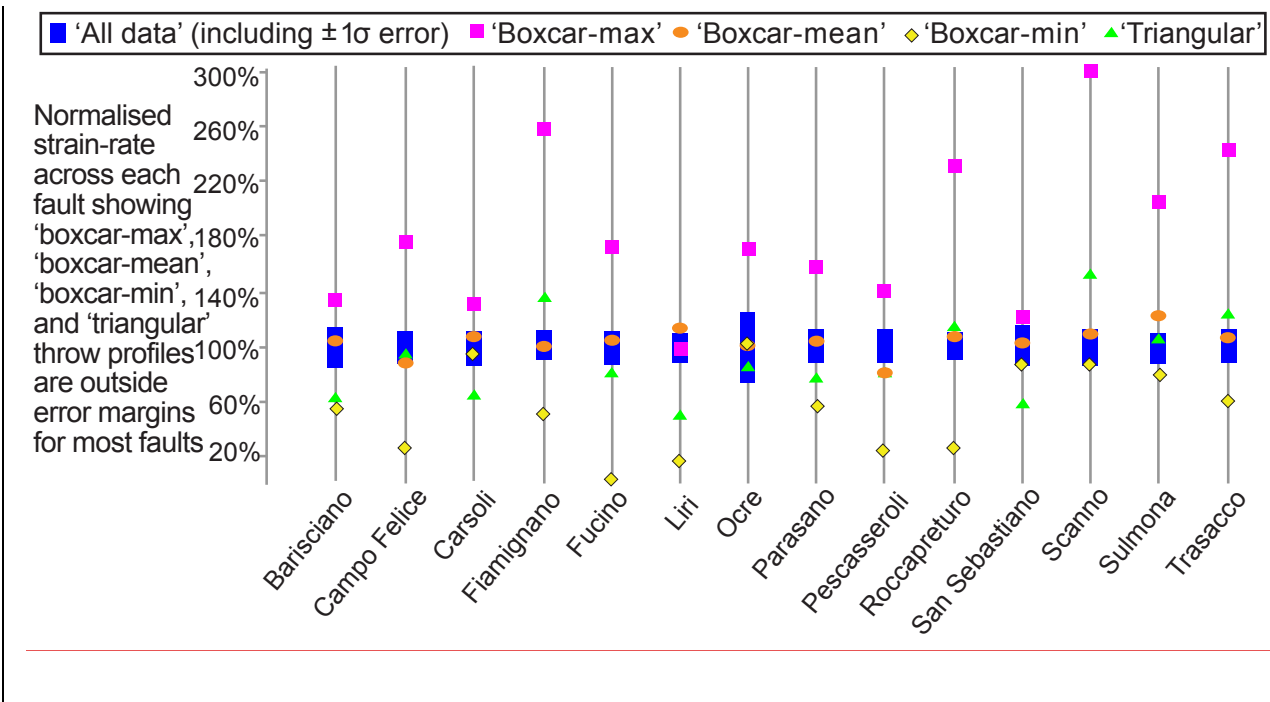
848

849 *Figure 5: Strain-rates calculated across 14 faults using different throw-rate profiles: 'all data'*

850 *case (blue rectangles including ±1σ), 'boxcar-max' (pink squares), 'boxcar-mean' (orange*

851 *ovals), 'boxcar-min' (yellow diamonds) and 'triangular' (green triangles). The strain-rates*

852 *calculated using simplified throw-rate profiles are shown relative to those calculated using the*

853 *'all data' throw-rate profiles. The inferred strain-rates calculated using simplified throw-rate*

854 *profiles mostly lie outside ±1σ uncertainty of the 'all data' strain-rates, demonstrating that the*

855 *simplified throw-rate profiles are insufficient for calculating strain-rates across faults.*

Annual occurrence rates

Mw≥5.1 Recurrence rates
(i) 'All data' (420yrs)
(ii) 'No max' (465yrs)
(iii) 'Boxcar-max' (262yrs)
(iv) 'Triangular' (524yrs)

Figure 6: Frequency-magnitude semi-log plots for M_w 4.9-5.5 for the four throw-profile scenarios along the Parasano-Pescina fault. The graphs compare the (i) all data sites included in the 'all data' throw profile with three sets of degraded data. The three sets of degraded data are created by: (ii) leaving out the maximum throw point in the 'no max' profile but including the other measurements; (iii) extrapolating the maximum throw along the whole fault in a 'boxcar-max' profile; and (iv) extrapolating throw along the fault by decreasing the maximum throw linearly to the fault tips in a 'triangular' profile. Calculated earthquake $\geq M_w 5.1$ recurrence intervals are 420yrs, 465yrs, 262yrs and 524yrs for cases (i) – (iv) respectively. This example shows that using simplified throw-rate profiles can change calculated recurrence intervals that are used to inform PSHA.
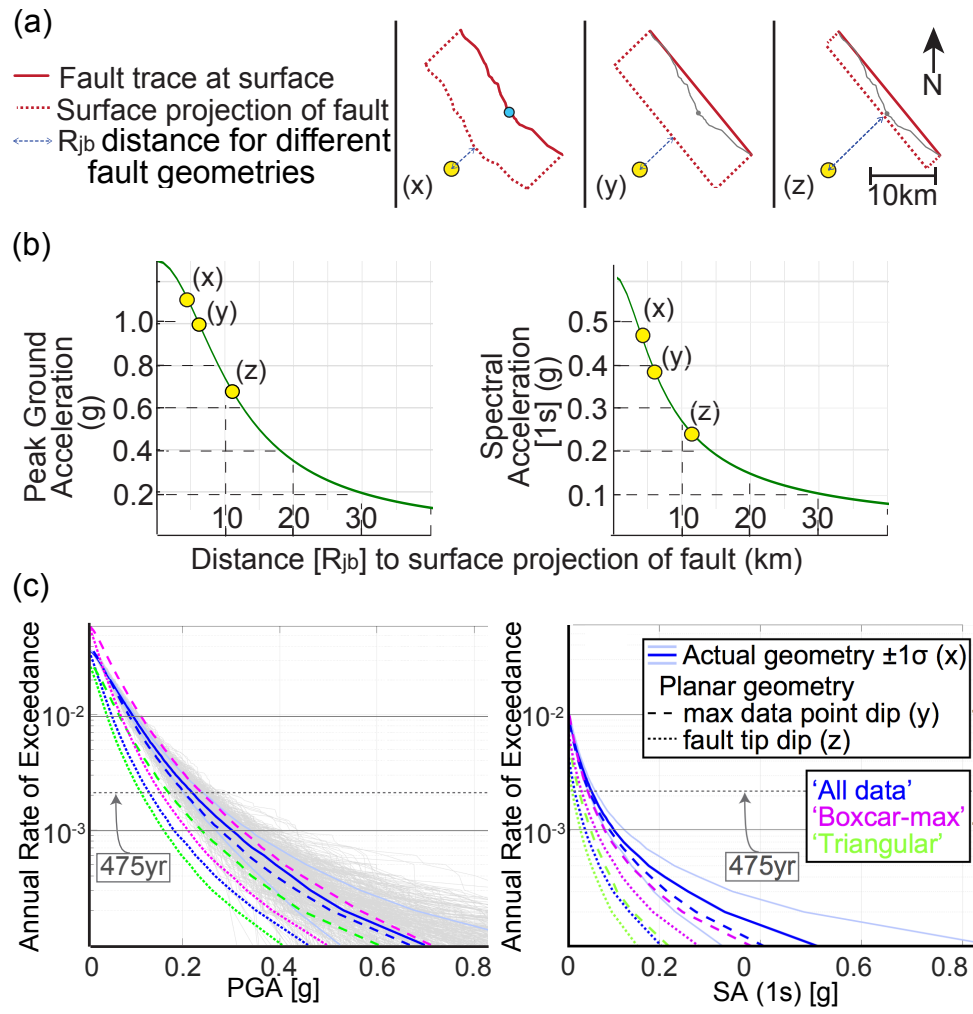
Figure 7: Effect of using simplified geometry and displacement-rate profiles on annual rates of exceeding specified ground shaking intensities. The figure shows that ignoring fault bends and measured dips changes calculated shaking beyond 1σ uncertainty. (a) Maps show actual fault geometry (x) and surface projection of fault assuming the depth of the seismogenic layer is 15km and non-listric geometry with depth. The example site, Valle Massima, is shown as a yellow circle. The R_{jb} distance to the example site is 4.6km (x) (apparent dip of fault at (x) is 55°), but this distance is increased to 6.4km and 11.3km if the fault is simplified to having planar geometry between the tips with the dip projected from the maximum throw-rate site (y) (55° apparent dip) and tip (z) (81° apparent dip) respectively. (b) The graphs show how the R_{jb}

877 *distance affects peak ground acceleration and spectral acceleration with distances (x), (y) and*

878 *(z) shown, using GMPEs from Bindi et el. (2011). (c) Annual rates of exceedance against peak*

879 *ground acceleration (PGA) and spectral acceleration (SA) from earthquakes on the Pescasseroli*

880 *fault at the given example site, Valle Massima. PGA and SA are calculated for the 'all data'*

881 *throw profile for fault-to-site distances (R_{jb}) based on detailed fault geometry ((x), blue solid*

882 *line, ±1σ uncertainty shown with paler blue solid lines). Grey lines show each of the 500*

883 *simulation lines run for the PGA calculations. Ground shaking is further calculated using*

884 *simplified planar fault geometries using a straight fault trace from tip-to-tip and fault dip*

885 *projected from the maximum throw data site ((y), dashed line) and dip at the fault tip ((z), dotted*

886 *line). The simplified fault geometry source-to-site distances are also combined with recurrence*

887 *rates calculated for the 'boxcar-max' (pink lines) and 'triangular' (green lines) throw-profiles to*

888 *show the combined effect of simplifying throw profiles and using simplified geometries. In this*

889 *example, using a simplified throw-rate profile and planar fault geometry gives lower values of*

890 *calculated ground shaking intensities than using the actual values and therefore may*

891 *underestimate the seismic hazard to a region or town.*